RSC Advances

PAPER

View Article Online
View Journal | View Issue

Cite this: *RSC Adv.*, 2014, **4**, 6407

Effect of carbon coating on the electrochemical properties of Co_2SnO_4 for negative electrodes in Li-ion batteries

S. Yuvaraj,[a] S. Amaresh,[b] Y. S. Lee[b] and R. Kalai Selvan*[a]

Received 12th November 2013
Accepted 20th December 2013

DOI: 10.1039/c3ra46588h

www.rsc.org/advances

Co_2SnO_4 particles were synthesized by a sonochemical method under different pH conditions, followed by carbon coating by a hydrothermal method. The thermal stability and compound formation temperature were identified through thermogravimetric analysis (TGA). The X-ray diffraction (XRD) pattern elucidated the compound formation of Co_2SnO_4 with cubic structure. Co_2SnO_4 encapsulated with carbon was confirmed through the TEM and HRTEM analysis and the approximate thickness of carbon was around 20 nm. The pristine-Co_2SnO_4 and carbon coated Co_2SnO_4 provided a discharge capacity of 777 mA h g^{-1} and 780 mA h g^{-1} at the current density of 40 mA g^{-1} with the capacity retention of 67% and 81% respectively in the 20th cycle. The charge transfer resistance of carbon coated Co_2SnO_4 was low when compared to pristine Co_2SnO_4 which lead to good reversibility of the material. The electrochemical study revealed the excellent electrochemical performance of the carbon coated Co_2SnO_4 particles with superior cycling stability and electronic conductivity.

1. Introduction

Rechargeable Li-ion batteries are emerging electrochemical energy storage devices which are widely used in different applications such as cell phones, laptops and digital cameras. Commercially used Li-ion batteries consist of $LiCoO_2$ and graphite as cathode and anode, respectively. Li-ion batteries have several advantages such as high energy density, high operating voltage, low self-discharge, light weight and no memory effect. However, the use of Li-ion batteries in electric vehicles, hybrid electric vehicles and plug in hybrid electric vehicles is limited since it requires high power density, high rate capability and good cycling performance. So, in order to improve these kinds of properties, finding new electrode material is necessary. Commercially used graphite has several advantage such as low and flat working potential, long cycle life and low cost. On the other hand, it reduces the battery performance in terms of energy and power density due to the theoretical capacity of Graphite (372 mA h g^{-1}) and low Li-ion transport rate (always less than 10^{-6} cm^2 s^{-1}) respectively.[1] To enhance the electrochemical performance of Li-ion batteries, identifying potential negative electrode is mandatory, especially the materials having high theoretical capacity and higher Li diffusion rates. Currently, metals (Sn, Si, Sb and Ge), metal oxides (SnO_2, TiO_2) and transition metal oxides, MOx (M = Zn, Co, Ni, Mn) are focused as anode materials for Li-ion batteries because of their higher energy densities. The alloy anodes possess low operation potential *vs.* Li/Li^+, higher volumetric and gravimetric energy densities due to its alloying and de-alloying mechanism and good safety. However, this material shows poor capacity retention due to its alloying/de-alloying process, which causes a huge volume expansion and leads to deterioration of active materials.[2,3] The SnO_2 material shows similar electrochemical reactions as that of Sn after the first cycle, delivering a high theoretical capacity of ~790 mA h g^{-1} corresponding to the $Li_{4.4}Sn$. In the first cycle, Li bonds to the oxygen in SnO_2 to form Li_2O, after that Sn starts alloying with lithium and this alloying and de-alloying process continuous for further repetitive cycling. But SnO_2 shows a rapid capacity fading due to its tremendous volume changes, up to 200–300% upon alloying and de-alloying process, which initiates the pulverization of electrodes and loss of electrical contact between the active materials after repeated cycling.[3] The transition metal oxides MO_x (M = Mn, Co, Ni, Fe) exhibits high reversible capacities and high energy densities because of the nature of conversion reaction mechanism where more than one electron involves in the electrochemical reaction. However, it suffers from poor kinetics because of their inherent nature of low electrical conductivity, poor capacity retention and unstable solid electrolyte inter phase formation at high current densities that is mainly because of the large volume changes during insertion/de-insertion process.[4]

In recent years spinel like structures are widely investigated as anode materials for Li-ion batteries especially MCo_2O_4,[5–7]

[a]*Solid State Ionics and Energy Devices Laboratory, Department of Physics, Bharathiar University, Coimbatore-641 046, India. E-mail: selvankram@buc.edu.in; Fax: +91 422 2425706; Tel: +91 422 2428446*

[b]*Faculty of Applied Chemical Engineering, Chonnam National University, Gwangju 500-757, Korea*

MMn_2O_4,[8,9] MFe_2O_4,[10,11] and M_2SnO_4 (M = Zn, Co, Ni, Mn, Ca).[12–16] On the other hand, $CoSnO_3$ based compounds also showed better performance than the ball-milled mixtures of CoO/SnO_2.[17,18] Further, Co_3O_4@SnO_2@C core shell nanorods showed excellent cycling stability at a current density of 200 mA h g^{-1}.[19] Overall, spinel based electrodes delivered good rate capability and cycling stability due to its nature of storage mechanism.[8,20] As well as the Co_2SnO_4 structure containing excess Co content leads to better cycling stability than the $CoSnO_3$ anodes.[21] Therefore, we have chosen the spinel like structure, Co_2SnO_4 compounds which shows higher theoretical capacity (1105 mA h g^{-1}) and exhibits both Li-ion insertion/de-insertion and alloying/de-alloying mechanism while charging and discharging.[16] This kind of mixed reaction mechanism may be improving the energy density of the material. However, a scarce amount of work is available for Co_2SnO_4, like those synthesized by hydrothermal, sol–gel and co-precipitation methods as anodes.[16,22–25] Here, we have synthesized Co_2SnO_4 by sonochemical method and the compound formation is studied with respect to change in concentration of LiOH. The electrochemical performance is analyzed for the optimized Co_2SnO_4 particles and further to improve the cycling stability and coulombic efficiency of the active material, the core–shell structure of Co_2SnO_4@C is prepared using hydrothermal method, where glucose acts as a carbon source. The core–shell structure has several advantages such as enhancement of electronic conductivity of the electrode material, protect the core from the electrolyte, restrict the volume expansion during cycling and maintain structural stability of the active material.[26]

2. Experimental methods and materials

2.1 Synthesis of Co_2SnO_4 by sonochemical method

Co_2SnO_4 particles were prepared by sonochemical method. The starting precursors are $CoCl_2 \cdot 6H_2O$, $SnCl_4 \cdot 6H_2O$ and LiOH purchased from the Merck Specialties Private limited, Mumbai. Stoichiometric amounts of 1.563 g of $CoCl_2 \cdot 6H_2O$ and 1.166 g of $SnCl_4 \cdot 5H_2O$ were dissolved into 25 ml of water individually. Then the $CoCl_2 \cdot 6H_2O$ solution was subjected in to a sonochemical set up (Ultrasonic Cell Crusher, Frequency 22 kHz and 950W output power). Simultaneously, $SnCl_4 \cdot 5H_2O$ solution was added drop wise into $CoCl_2 \cdot 6H_2O$ solution under sonication. Subsequently, 1.863 g of LiOH was added drop wise in to the above solution; the obtained precipitate was sonicated for 2 hours. The obtained gray color precipitate was centrifuged and dried at 80 °C for 12 hours. The dried sample was ground for 15 minutes and then finally calcined at 950 °C for 5 hours to obtain single phase green color Co_2SnO_4 particles.

2.2 Synthesis of Co_2SnO_4@C by hydrothermal method

The carbon coated Co_2SnO_4 was prepared by using hydrothermal process and glucose act as a carbon source. The prepared Co_2SnO_4 (0.4 g) particles was dispersed into 0.25 M of aqueous glucose solution. The above solution was transferred into a 75 ml Teflon-lined stainless steel autoclave, sealed and maintained at 180 °C for 12 h. After the reaction got over, the solid product was washed several times with distilled water and ethanol to remove the organic products and the remaining ions from the residue. The sample was dried at 80 °C for 12 h under air atmosphere. Finally, for carbonization process the product was heat treated at 500 °C under Ar atmosphere.

2.3 Electrode preparation and characterization techniques

Electrochemical characterizations of all the synthesized materials were performed using a CR2032 coin cell. The cell consisted of synthesized material as working electrode and a metallic lithium foil as counter electrode separated by a polypropylene separator with 1 M $LiPF_6$ dissolved in ethylene carbonate–dimethyl carbonate (EC : DMC) 1 : 1 (v/v) as electrolyte. The working electrodes were prepared with active material, Ketzen black (KB) as conductive additive and teflonized acetylene black (TAB) as binder in the ratio of 72 : 14 : 14 (wt%) using ethanol as solvent. The resultant electrode film was pressed over a stainless steel current collector, followed by drying at 160 °C for 4 h before being used in the cell. The average loading of the cells were maintained at ~5 mg cm^{-2}.

X-Ray Diffraction analysis was characterized using XPERT-PRO diffractometer with Cu-Kα (1.5406 Å) source and step size was fixed at 0.02°. TG/DTA was carried out using Pyris 1 TGA model instrument with temperature range from 30 °C to 950 °C at heating rate of 5 °C min^{-1} and nitrogen gas flow rate at 20.0 ml min^{-1}. Fourier transform infra-red spectroscopy (FTIR) technique was carried out using Bruker Tensor 27 model with wavenumber range of 400–4000 cm^{-1}. Raman analysis was performed on carbon coated sample using Renishaw invia Raman microscope instrument using He–Ne laser (633 nm) as excitation source in the wavenumber range of 600–2000 cm^{-1}. XPS analysis was carried out to analyze the oxidation state using XPS, Krato Analytical, Ultra axis instrument. The morphological features were analyzed using JEOL JEM 2100 High resolution transmission electron microscope (HRTEM). Cyclic voltammetry (CV) and electrochemical impedance spectroscopy (EIS) studies were carried out using an electrochemical work station (SP-150, Biologic, France) at room temperature. The EIS spectra were measured in the frequency range between 100 kHz and 100 mHz using an applied current amplitude of 100 μA, while the CV was tested at a scan rate of 0.5 mV s^{-1} between the operating voltage of 0 V and 3.0 V with lithium being both a counter and reference electrode. Galvanostatic charge–discharge test was carried out with a battery tester (WBCS 3000, Won-A-Tech, Korea) in the voltage range of 0–3 V at 40 mA g^{-1}.

3. Results and discussion

3.1 XRD analysis

XRD pattern of Co_2SnO_4 particles prepared using different concentration of LiOH is shown in Fig. 1. It is well known that the formation of single phase is mainly depends upon the pH or alkaline concentration of the precursor solution. Fig. 1(a) shows the XRD pattern of 8 M LiOH (pH = 10) used Co_2SnO_4, where two different phases of SnO_2 and Co_2SnO_4 is observed.

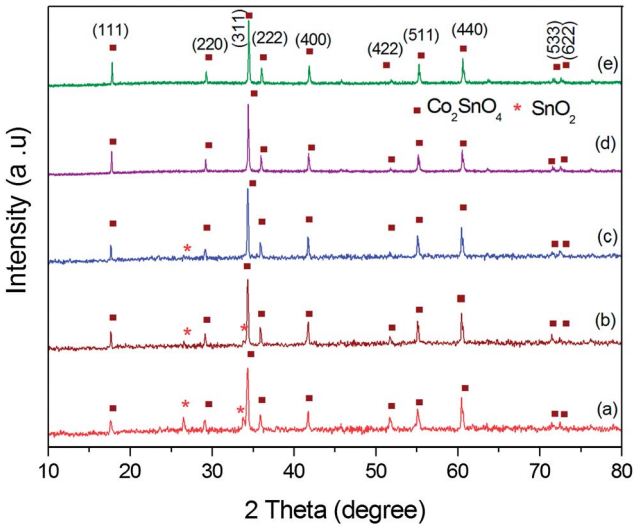

Fig. 1 XRD patterns of 950 °C calcined Co_2SnO_4 prepared at different concentration of LiOH. (a) 8 M, (b) 10 M, (c) 12 M, (d) 14 M, (e) 16 M.

However, the high intensity peaks are well matched with the Co_2SnO_4 phase (JCPDS file no. 29-0514) and the rest of the peaks matched with SnO_2 phase (JCPDS File no. 88-0287). Subsequently, more prominent Co_2SnO_4 phase and suppressed reflection of SnO_2 phase is observed for using 10 M and 12 M LiOH solution (Fig. 1(b and c)). On the other hand, Fig. 1(d and e) elucidates the formation of single phase Co_2SnO_4 while using 14 M and 16 M of LiOH. The observed reflections at 17.70°, 29.13°, 34.32°, 35.91°, 41.71°, 51.76°, 55.11°, 60.49°, 71.50° and 72.40° are indexed and well matched with the standard JCPDS file no. 29-0514. The sharp intensity peaks denoted high crystallinity of Co_2SnO_4. The calculated crystallite size, using Scherrer's equation, for the strong intensity peak (311) is 104 nm. Using CELREF software, the lattice constant ($a = 8.6298$ Å) and cell volume (642.6832 Å^3) are calculated and are in good agreement with the standard JCPDS file no. 29-0514.

From the above observations, the XRD pattern clearly indicated that SnO_2 formation is more prominent at lower pH, than that of Co_2SnO_4 since the Sn^{4+} ions are easily hydrolyzed and forms $Sn(OH)_4$ precipitates at low pH (~3–4). So higher pH or strong alkaline environment is necessary to form $Co(OH)_2$. According to eqn (1), the hydrolysis constant of aqua complexes determines the precipitation process that mainly depends upon the charge and electronegativity of the cations.[27]

$$pK_a = 15.14 - 0.8816\left\{\frac{Z^2}{r} + 9.60(\chi_{pauling} - 1.50)\right\} \quad (1)$$

where, Z is the charge of the ion, r is the ionic radius and $\chi_{pauling}$ is the Pauling electronegativity of the ion. Actually the precipitation starts when only the solution pH approximately equals to the hydrolysis constant of pK_a values. The calculated pK_a values of the Co^{2+} and Sn^{4+} ions are −0.6 and 9.6, respectively,[28] which means the Sn^{4+} ions are strong acids compared to Co^{2+} ions. This may be due to the inductive effect of Sn^{4+} ions. This highly charged Sn^{4+} ion has large polarizing power and strongly pulls the lone pair of electrons from the oxygen atom and weakens the O–H bond.[29] Due to large polarizing power of Sn^{4+} ions, the electron density from the coordinated water molecules is withdrawn to the empty p-orbital of Sn^{4+} cation and the solution becomes more acidic. So in the presence of mild basic condition Sn^{4+} ions gets hydrolyzed and gives way for the $Sn(OH)_4$ formation according to the eqn (2) and (3),

$$[Sn(H_2O)_6]^{4+} + H_2O \rightarrow [Sn(OH)(H_2O)_5]^{3+} + H_3O^+ \quad (2)$$

$$[Sn(OH)(H_2O)_5]^{3+} + 3OH^- \xrightarrow{pH<4} [Sn(OH)_4(H_2O)_2] + 3H_2O \quad (3)$$

$$[Co(H_2O)_6]^{2+} + 2OH^- \xrightarrow{pH>8} [Co(OH)_2(H_2O)_4] + 2H_2O \quad (4)$$

According to partial charge model,[30] when the two atoms present in the solution has different electronegativity, both the atoms tend to equalize the electronegativity in the solution. So based on the equalization principle, the deprotonation of water molecules will takes place until the electronegativity of the $[Co(H_2O)_6]^{2+}$ precursor solution is equal to the surrounding water molecules. When pH increases by adding excess of LiOH, it facilitates charge transfer to take place from the 'σ' electrons of coordinated water molecules to the empty d orbital of Co^{2+} ions, which reduces the positive charge of the aqua complex of cobalt ions. The complete formation $Co(OH)_2(H_2O)_4$ (eqn (4)) occurred at strong alkaline environment when the electronegativity of the aqua complex of cobalt(II) ion is equal to the electronegativity of the aqueous solution. This equilibrium condition is called as the isoelectric point. In this equilibrium condition, protons are delocalized in the hydrogen bonds on the aqueous solution. So, the rate of hydrolysis of hydrated cation mainly depends on the charge and electronegativity of the metal cation.

3.2 TG/DTA analysis

The compound formation temperature, thermal decomposition as well as the percentage of carbon in the Co_2SnO_4@C is identified through TG/TDA analysis. Fig. 2 shows the TGA curve of as prepared Co_2SnO_4 particles, which indicates six different weight loss in the measured temperature range. The first weight loss occurred from room temperature to 160 °C is due to evaporation of physically adsorbed water molecules (eqn (5a) and 5b). The observed second weight loss in the temperature range between 160 °C and 219 °C corresponds to the dehydroxylation of hydrotalcite structure of cobalt hydroxide into brucite phase of cobalt hydroxide, further confirmed from the exothermic peak at 217 °C in DTA curve.[31] The dehydroxylation of brucite phase of cobalt hydroxide converted into Co_3O_4 (eqn (6)) at 219 °C to 270 °C (third weight loss) which is also well consistent with the DTA curve and it clearly indicates the exothermic reaction of cobalt hydroxide at 267 °C.[32] The obtained fourth weight loss (280 °C to 700 °C), attributes to the phase changes from H_2SnO_3 to tin oxide (eqn (7)).[33] This phase change was substantiated by the DTA curve, where the exothermic peak at 650 °C corresponds to the removal of water from the H_2SnO_3. Subsequently, the Co_3O_4 phase transformed into CoO phase at 750 °C to 850 °C, (eqn (8)) and DTA also confirms the exothermic reaction at

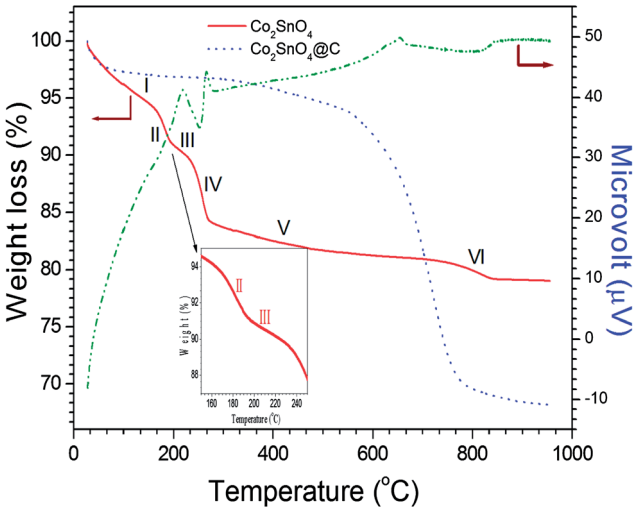

Fig. 2 TG/DTA curve of Co_2SnO_4 (a) and magnified image of II and III region (inset) and TGA curve of Co_2SnO_4@C.

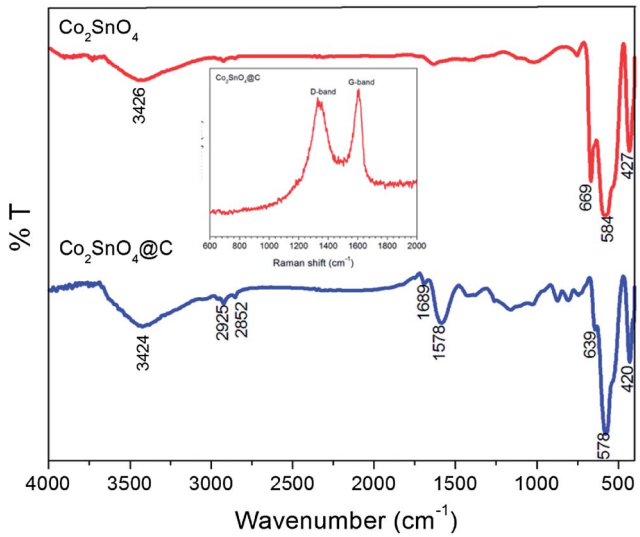

Fig. 3 FT-IR spectra of Co_2SnO_4 and Co_2SnO_4@C and Raman spectrum of Co_2SnO_4@C (inset).

840 °C for the transition of CoO from Co_3O_4. Finally, there is no weight loss occurred at above 850 °C, which assured the diffusion of CoO and SnO_2 into their lattices to form Co_2SnO_4 particles at the temperature range of 850 °C to 900 °C according to eqn (9). From the TG/DTA analysis, the compound formation was confirmed at 900 °C, so calcination temperature was fixed at 950 °C in order to improve the crystallinity and prevent the formation of impurities such as SnO_2 and CoO. Fig. 2 shows the TGA curve of the carbon coated Co_2SnO_4 sample. As mentioned earlier, TGA can be used to identify the amount of carbon present in Co_2SnO_4. The weight loss occurred around at 400 °C to 700 °C which denotes the evaporation of carbon from the surface of the active material. The TGA analysis confirms that 27 wt% of carbon is coated on the surface of the Co_2SnO_4 particle.

$$[Co(OH)_2(H_2O)_4] \rightarrow Co(OH)_2 + 4H_2O \quad (5a)$$

$$[Sn(OH)_4(H_2O)_6] \rightarrow H_2SnO_3 + 7H_2O \quad (5b)$$

$$3Co(OH)_2 \rightarrow Co_3O_4 + 2H_2O + H_2 \quad (6)$$

$$H_2SnO_3 \rightarrow SnO_2 + H_2O \quad (7)$$

$$Co_3O_4 \rightarrow 3CoO + 1/2O_2 \quad (8)$$

$$2CoO + SnO_2 \rightarrow Co_2SnO_4 \quad (9)$$

3.3 FT-IR analysis

The FT-IR spectra of Co_2SnO_4 and Co_2SnO_4@C are given in Fig. 3. Both the spectrum explains the functional group of Co_2SnO_4 observed at the wavenumbers of 427 cm^{-1}, 584 cm^{-1} and 669 cm^{-1}. The sharp absorption peak at 427 cm^{-1} corresponds to the stretching vibration of Co–O bond.[34] The broad absorption band at 584 cm^{-1} and 669 cm^{-1} was assigned to the asymmetric vibration of Sn–O–Sn bond.[35,36] The broad and weak absorption band observed around 3426 cm^{-1} is ascribed to the symmetric stretching vibration of –OH groups due to the presence of adsorbed moisture. Fig. 3 shows the carbon coated Co_2SnO_4 sample which indicates a new absorption peak at 1578 cm^{-1} and 1689 cm^{-1} ascribed to the stretching vibration of C=C bond and stretching vibration of C=O. This elucidates the aromatization of glucose around the Co_2SnO_4 sample converting into carbon layer during the thermal treatment at an inert atmosphere. Absorption peaks at 2852 cm^{-1} and 2925 cm^{-1} corroborates the symmetric and asymmetric stretching vibration of C–H bond respectively.[37–39]

Raman analysis was carried out to ensure the nature of carbon coating on the surface of the active material. Fig. 3 (inset) shows the Raman spectra of carbon coated Co_2SnO_4 which clearly indicates the two broad peaks at 1330 cm^{-1} and 1605 cm^{-1}. The broad peak at 1330 cm^{-1} (D-band) corresponds to disorder induced along the c-axis of graphitic carbonaceous material and 1605 cm^{-1} (G-band) reveals the vibration of sp^2 hybridized carbon atoms in graphitic carbon.[40,41] The D and G band reveals the degree of crystallinity of the carbonaceous materials.[42] The calculated I_D/I_G ratio was 0.83 which indicates the highly disorder nature of the carbon layer and high contribution of sp^3 hybridized disordered carbon.

3.4 XPS analysis

The XPS analysis further elucidates the carbon coating, chemical composition and oxidation state of Co_2SnO_4. Fig. 4(a) shows the full scan profile of C–Co_2SnO_4 in the region of 0–1000 eV. The peaks at 780.0 eV, 795.4 eV, 485.0 eV, 493.5 eV, 530.9 eV and 283.3 eV corresponding to the characteristic peaks of Co 2p, Sn 3d, O 1s and C 1s respectively, which clearly indicates the presence of cobalt, tin, oxygen and carbon atom in the prepared sample that are free from the impurities. Fig. 4(b) shows the Co 2p region and it deconvoluted peaks, which represents the two sharp peaks. The sharp peak at 780.0 eV and 795.4 eV

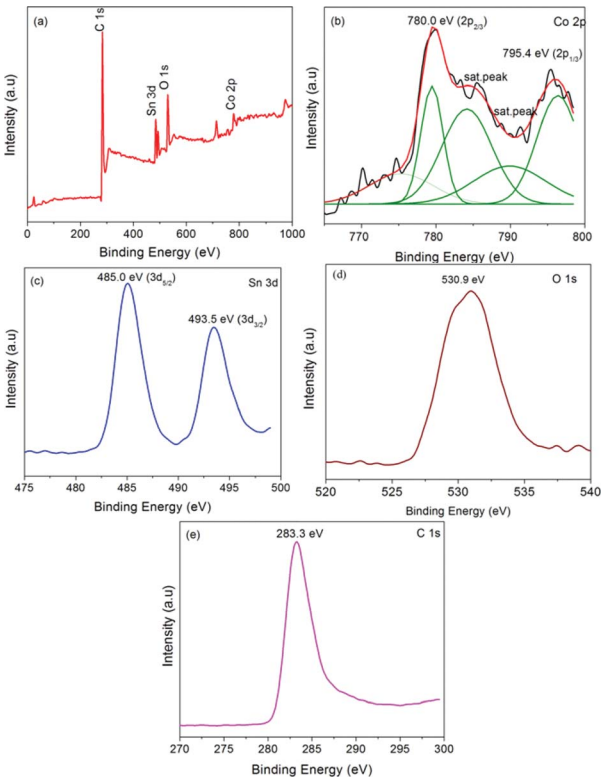

Fig. 4 XPS spectra of Co_2SnO_4@C: (a) survey spectrum, (b) Co 2p, (c) Sn 3d, (d) O 1s and (e) C 1s spectra.

corresponds to the binding energy of spin-orbit doublets of $2p_{3/2}$ and $2p_{1/2}$. The binding energy separation of the spin-orbit doublet is 15.4 eV which confirms the existence of Co^{2+} in the sample and the two satellite peaks at 785.5 eV and 788.7 eV is associated with the Co^{2+} and Co^{3+} respectively which is well consistent with previous reports.[6,43] Fig. 4(c) shows the Sn 3d region, the binding energy at 485.0 eV and 493.5 eV is related to the $3d_{5/2}$ and $3d_{3/2}$ and the value of binding energy separation is 8.5 eV.[44] Fig. 4(b) and (c) reveals that the Cobalt exist in the 2+ and tin exist in the 4 + oxidation state in Co_2SnO_4 sample. Fig. 4(d) shows the O 2p region, the binding energy of 530.9 eV is ascribed to the metal-oxygen bonds.[45] Fig. 4(e) represents the C 1s spectrum with sharp and high intensity peak at 283.3 eV corroborating that the carbon is coated on the surface of the Co_2SnO_4 sample during carbonization process.

3.5 TEM and HRTEM analysis

Fig. 5(a) shows the TEM image of the pristine Co_2SnO_4 sample. The TEM image indicates that the particle seems to be non uniform in shape. The measured particle size was in the range of 0.2 μm to 0.42 μm. Fig. 5(b and c) reveals the TEM images of the Carbon coated Co_2SnO_4 and magnified image of the carbon coated sample which clearly shows a thick layer of carbon coating on the surface of the Co_2SnO_4 sample and thickness of the carbon layer is 15 nm (Fig. 5d). Fig. 5(e) shows the HRTEM image of the carbon coated Co_2SnO_4 sample which indicates the *d*-spacing value of 0.16 nm corresponding to the (511) plane of cubic phase of Co_2SnO_4 particles. Fig. 5(f) represents the SAED pattern of carbon coated Co_2SnO_4 sample.

The diffraction rings of the SAED pattern corroborates the polycrystalline nature of the sample and measured *d*-spacing values are 0.3219 nm, 0.2796 nm, 0.2093 nm, 0.1852 nm and 0.1622 nm and corresponding lattice planes are (220), (311), (400), (422) and (511), respectively. The *d*-spacing values were in

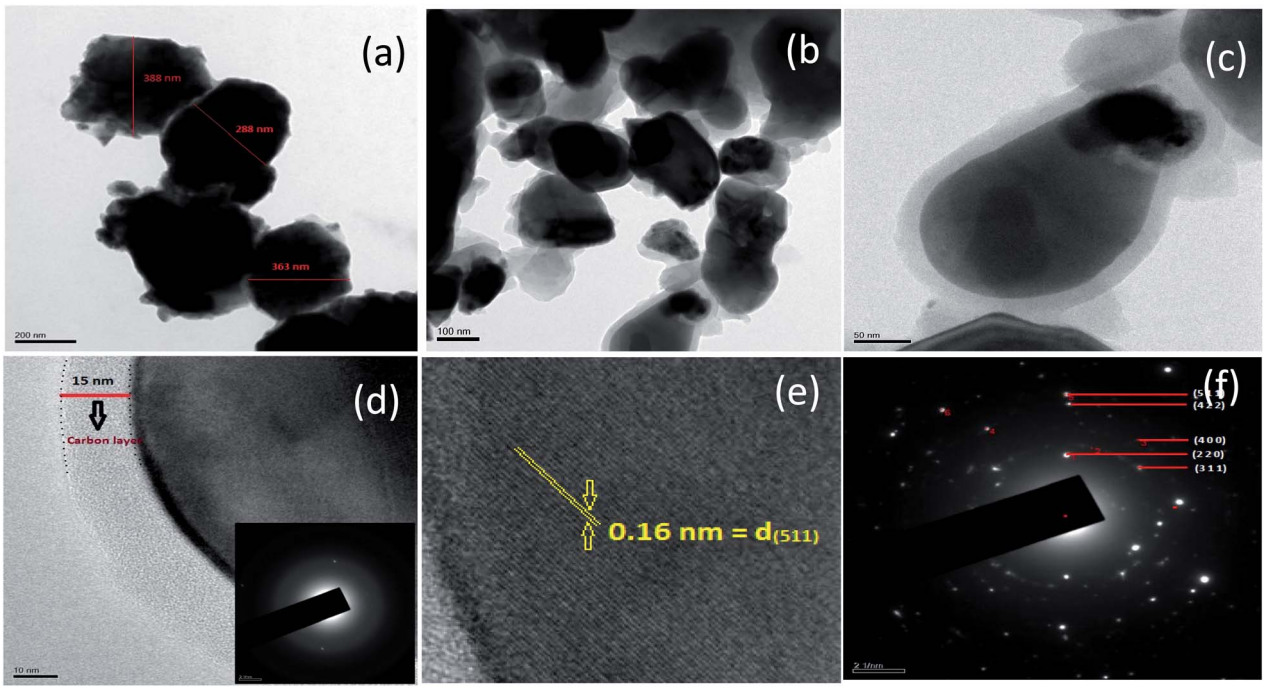

Fig. 5 TEM images of Co_2SnO_4 (a), Co_2SnO_4@C (b–e) and SAED pattern of Co_2SnO_4@C (f).

good agreement with the XRD results. SAED pattern of Co_2SnO_4@C (inset: Fig. 5(d)) shows the presence of hollow ring pattern and indicated the presence of amorphous carbon layer on the surface of Co_2SnO_4 particle.

3.6 Electrochemical studies

Electrochemical properties of Co_2SnO_4 and carbon coated Co_2SnO_4 particles are analyzed through cyclic voltammogram and galvanostatic charge–discharge curve. Cyclic voltammogram is a very useful technique that gives the relevant information about oxidation, reduction process and phase transformations during intercalation and de-intercalation process of Li^+ ions Fig. 6 shows the cyclic voltammogram of Co_2SnO_4 and Co_2SnO_4@C sample in the potential window of 0–3.0 V at a scan rate of 0.5 mV s^{-1}. In the first discharge process, a sharp reduction peak at 0.65 V or cathodic current is ascribed to the complex reaction taking place at electrode/electrolyte interface or electrolyte decomposition ($LiPF_6 \rightarrow LiF + PF_5$) and many other side reactions that can occur. This leads to the formation of passive solid electrolyte inter-phase film (SEI) on the surface of the active materials and decomposition of Co_2SnO_4 particles leads to the formation of amorphous Li_2O matrix,[46–48] which is indicated in eqn (10) and three anodic peaks were observed at 0.6 V, 1.4 V and 2.1 V which is ascribed to the de-alloying process of $Li_{4.4}Sn$, oxidation of metallic Sn to form SnO_2 and oxidation of Co to form CoO, respectively which is shown in eqn (11)–(13).[49,50]

$$Co_2SnO_4 + 8Li^+ + e^- \rightarrow 2Co + Sn + 4Li_2O \quad (10)$$

$$Sn + 4.4Li + 4.4e^- \leftrightarrow Li_{4.4}Sn \quad (11)$$

$$Sn + 2Li_2O \leftrightarrow SnO_2 + 4Li + 4e^- \quad (12)$$

$$Co + Li_2O \leftrightarrow CoO + 2Li^+ + 2e^- \quad (13)$$

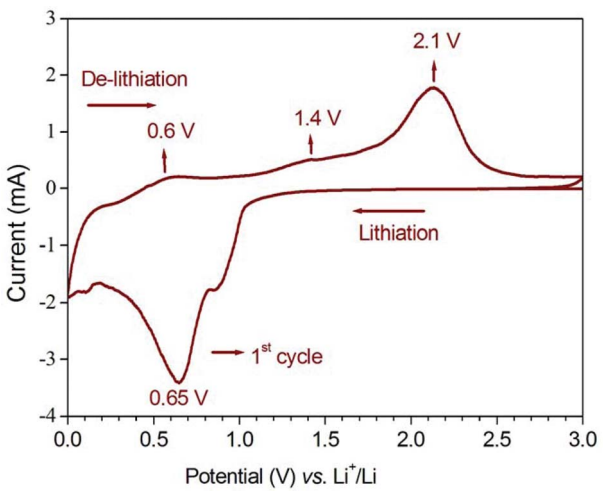

Fig. 6 Cyclic voltammogram of Co_2SnO_4 at scan rate of 0.5 mV s^{-1}.

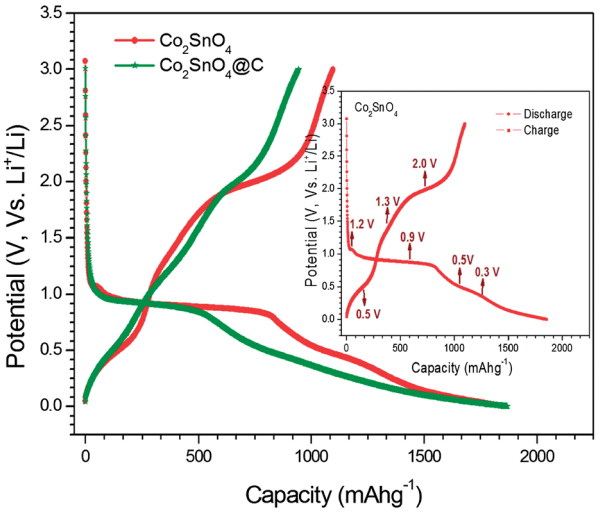

Fig. 7 Charge–discharge curve of Co_2SnO_4 and Co_2SnO_4@C.

Fig. 7 shows the charge–discharge curve of the Co_2SnO_4 and Co_2SnO_4@C in the potential window of 0 V–3.00 V at a current density of 40 mA g^{-1}. The discharge profile shows four plateau regions at 1.2 V, 0.9 V, 0.5 V and 0.3 V. The drastic voltage drop observed from the OCV and followed by short plateau region at 1.2 V corresponds to the lithium ion insertion[51] into the Co_2SnO_4 lattices and large plateau region around 0.9 V is associated with the reduction and irreversible reaction of Co_2SnO_4 along with the formation of lithium oxide matrix. The small plateau and sloping region at 0.5 V indicates the irreversible reaction of the active materials with the electrolyte. The discharge plateau below 0.3 V is ascribed to the Li–Sn intermetallic phase formation. During charging process three plateau region were observed at 0.5 V, 1.3 V and 2.0 V which is ascribed to the lithium extraction from the $Li_{4.4}Sn$, Sn oxidation and cobalt re-oxidation, respectively.[52] The results obtained from charge–discharge studies were well consistent with the CV results. The first discharge capacity of Co_2SnO_4 and Co_2SnO_4@C is calculated to be 1854 mA h g^{-1} and 1868 mA h g^{-1} respectively. The first discharge capacity of 1854 mA h g^{-1} corresponds to the consumption of 20 moles of Li as represented in eqn (10)–(13). The first discharge capacity is higher than theoretical capacity of 1105 mA h g^{-1} which is calculated from the consumption of 12.4 moles of Li in the reversible reaction ascribed to eqn (11)–(13). The large irreversible capacity observed due to decomposition of electrolyte, active material and the formation of solid electrolyte interphase and possible interfacial lithium storage due to charge separation at the metal-Li_2O phase boundary corresponds to eqn (10).[6,53] The first charging capacity is 1097 mA h g^{-1} and corresponds to a coulombic efficiency of 59%.

In second cycle, the charge and discharge capacities are 1102 mA h g^{-1} and 1155 mA h g^{-1} which results in enhancing coulombic efficiency at around 95% due to corresponding reversible reaction of alloying/de-alloying of Sn, oxidation and reduction of metallic Cobalt and Sn. In the second cycle, the charge and discharge capacities of carbon coated sample are

944 mA h g^{-1} and 959 mA h g^{-1} and its coulombic efficiency is 98% due to reversible reaction of eqn (11)–(13). The carbon coated Co_2SnO_4 sample shows a low discharge capacity when compared to that of pristine Co_2SnO_4. The reason behind this behavior is that carbon has theoretical capacity of 372 mA h g^{-1} and so the mass percentage of carbon content reduces the theoretical capacity of the active material. Theoretical capacity of the Carbon coated Co_2SnO_4 sample was calculated as.,[54]

$C_{theoretical} = C_{Co2SnO4}$ (mass percentage of Co_2SnO_4) + carbon (mass percentage of carbon) = (1105 mA h g^{-1} × 73%) + (372 mA h g^{-1} × 27%) $C_{theoretical}$ = 907 mA h g^{-1}.

Fig. (8) shows the discharge capacity *versus* cycle number of Co_2SnO_4 and Co_2SnO_4@C material at a current density of 40 mA g^{-1}. The pristine-Co_2SnO_4 sample shows a drastic discharge capacity loss from 1155 mA h g^{-1} to 777 mA h g^{-1} after 20 cycles with capacity retention of 67% and it exhibits poor capacity retention with repetitive cycling. But poor capacity retention is a general characteristics for metal oxides because during charging/discharging and alloying/de-alloying processes, volume expansion takes place which leads to the deterioration of the active material and improper electrical conduction between the active materials.[55] In case of carbon coated Co_2SnO_4 sample, a discharge capacity loss from 959 mA h g^{-1} to 742 mA h g^{-1} with capacity retention of 77% after 30 cycles shows the better reversible capacity. Qi *et al.* previously reported the different thickness of the carbon coating on Co_2SnO_4 particle on the application of Li-ion anode material and thickness of the carbon layer is 2–3 nm and 5–10 nm which shows the capacitance value of 550 mA h g^{-1} and 625 mA h g^{-1} at current density of 100 mA g^{-1} respectively.[22] But in our case, TEM image reveals that 10–15 nm range thickness of the carbon is coated on the active material which gives the better cycling performance and good reversible capacity when compared with previously reported carbon coated Co_2SnO_4 sample and the value is 780 mA h g^{-1} at current density of 40 mA g^{-1}. Our result substantiated the previous result and it is concluded that thickness of the carbon layer mainly determines the superior behavior of the material. During initial five cycles, the cycling stability decreases because of partial formation and decomposition of SEI film on the active material which reduces the coulombic efficiency of the material. After few cycles, the stable SEI film persist on the active material surface which act as a passivating layer and also restricts the direct interaction between the electrode and electrolyte and it facilitates the improvement of coulombic efficiency and cycling stability of the material. The cycling stability curve evidences that carbon coated Co_2SnO_4 sample delivers good capacity retention compared to that of pristine Co_2SnO_4 sample and thereby elucidates that carbon coating on the surface of the active material prevents the agglomeration of the active material and maintain their structural stability. At the same time, carbon coating keeps the electrical conduction between the active material as well as it acts as a buffering matrix during charging and discharging process.[56]

EIS is a technique that is used to analyze the electrode kinetic process as well as impedance of the cell. Impedance analysis shows the contribution of electrolyte resistance, surface film resistance and solid state diffusion of Li ions through the bulk of the active material. EIS analysis was carried out using fresh cell at open circuit voltage condition. Fig. 9(a) shows the Nyquist plot drawn between the real and imaginary

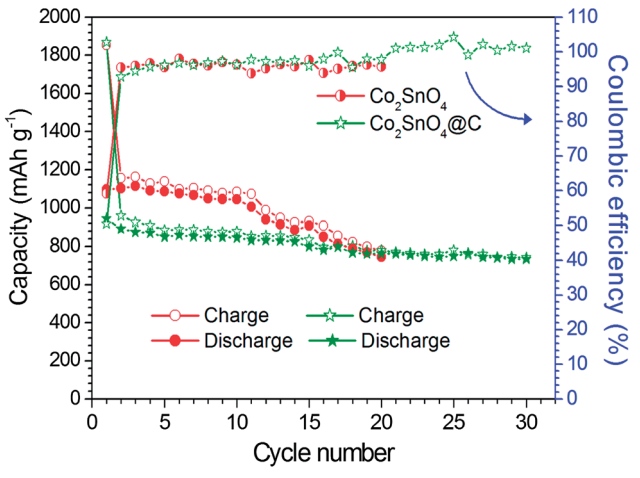

Fig. 8 Cycling stability and Coulombic efficiency of Co_2SnO_4 (20 cycles) and Co_2SnO_4@C (30 cycles) at current density of 40 mA g^{-1}.

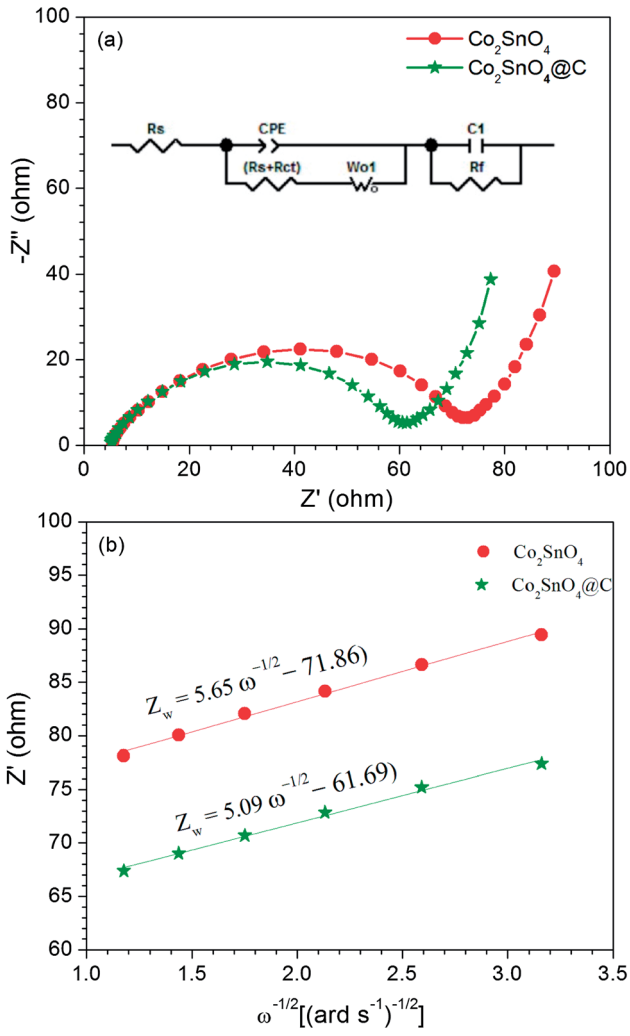

Fig. 9 (a) The EIS spectra of Co_2SnO_4 and Co_2SnO_4@C and their corresponding equivalent circuits (inset) and (b) Randles plot of Co_2SnO_4 and Co_2SnO_4@C.

Table 1 Fitting values of EIS spectra

Sample Name	R_s (Ω)	$R_{(sf+ct)}$, (Ω)	CPE (μF)	σ (Ω $s^{-1/2}$)	$D_{Li+} \times 10^{-14}$ (cm^2 s^{-1})
Co_2SnO_4	4.9	68.3	83.3	5.65	1.97
Co_2SnO_4@C	4.7	56.4	62.8	5.09	2.43

part of the resistance measured at frequency range of 100 kHz to 100 mHz. The Nyquist plot shows three regions. (i) A high frequency region (above 20 kHz), which is contributed by the ionic conduction through the electrolyte and it shows the pure resistive behavior because of Z_{img} part close to zero and there is no contribution of constant phase elements. (ii) Middle frequency region or semicircle (10 kHz to 10 Hz) indicates the charge transfer process through the solid electrolyte interphase film. (iii) The low frequency region (below 10 Hz) corresponds to the diffusion of Li^+ ions to the active material and semi infinite diffusion element due to the presence of the metallic current collector interface which blocks the diffusion of Li^+ ions.[57]

The experimental EIS spectra was fitted with an equivalent electrical circuit model and it is shown in inset Fig. 9(a) which consist of various circuit elements in series connection consisting of R_s, $R_{(sf+ct)}$//CPE_1, R_f//C_1 and W_{01}. Here, R_s is the electrolyte resistance, $R_{(sf+ct)}$ is the surface film and charge transfer resistance, CPE is the constant phase elements which is due to roughness and inhomogeneity of the electrode, R_f is the polarization resistance, C_1 is the intercalation capacitance and W_{01} is the Warburg impedance. EIS fitting values are shown in table 1 which indicates that electrolyte resistance (R_s) is almost same, but different values of $R_{(sf+ct)}$ determines the performance of the active material. The $R_{(sf+ct)}$ values of Co_2SnO_4 and Co_2SnO_4@C are 68.3 Ω and 56.4 Ω, respectively. Generally electrochemical performance of the active material mainly depends on the thickness of the SEI film and grain–grain boundary condition.[58] In the present case, thickness of the SEI film determines the electrochemical activity of the sample. At middle frequency region, Co_2SnO_4 sample shows the higher $R_{(sf+ct)}$ values as compared to carbon coated Co_2SnO_4 sample.

The higher R_{SEI} value is attributed to the formation of thick SEI film on the surface of the active material because pristine Co_2SnO_4, often exposed to the electrolyte, results in continual formation of very thick SEI films. This impedes the charge transfer and diffusion process of Li^+ ions and it consumes the Li^+ ions during intercalation and de-intercalation process that leads to capacity fading and low Coulombic efficiency.[59] On the other hand, carbon coated Co_2SnO_4 shows the low R_{SEI} value indicating the lesser thickness of the SEI film formed as compared to pristine one. Since carbon coating is to prevent the direct electrode–electrolyte interaction, it restricts the continuous rupturing and reformation of SEI film and thereby makes a stable SEI film formation on the surface of the carbon. The stable formation of SEI film reduces the thickness of the SEI film and shows the lower charge transfer resistance between electrode-electrolyte interfaces which increases the coulombic efficiency of the active material.[60] And also lower charge transfer resistance of carbon coated Co_2SnO_4 sample could enhance the kinetics of the material.[61]

EIS is also used to evaluate the diffusion coefficient of Li^+ ions on the active material. The diffusion coefficient calculated by the following eqn (14),[62]

$$D_{Li+} = R^2T^2/2A^2n^4F^4C^2\sigma^2 \quad (14)$$

where, n is the number of electrons per molecules during oxidation, A is the surface area of the active material, D is the diffusion coefficient of lithium ion, R is the gas constant, T is the absolute temperature, F is the Faraday constant, C is the concentration of lithium ion and σ is the coefficient of the Warburg impedance. 'σ' value is calculated from the slope of the linear plot between the real part of the impedance (Z') and inverse square root of the frequency ($\omega^{-1/2}$) at low frequency region or Warburg region (1–0.1 Hz) which is shown in Fig. 9(b). Since the diffusion of Li^+ ions taking place in the active material can be calculated from the data obtained at low frequency region at a phase angle of 45° to the real axis. The coefficient of Warburg impedance (σ) is related to Warburg factor and is given by eqn (15),

$$Z_w = R_s + R_{ct} + \sigma\,\omega^{-1/2} \quad (15)$$

The calculated value of diffusion coefficient of Li^+ ions is 1.97×10^{-14} cm^2 s^{-1} and 2.43×10^{-14} cm^2 s^{-1} corresponding to the Co_2SnO_4 and carbon coated Co_2SnO_4 sample. The diffusion coefficient is lower for pristine Co_2SnO_4 and increases after coating on the carbon to the pristine Co_2SnO_4. The higher diffusion coefficient of Core-shell structure increases the electrode kinetics of the Li^+ ions. From this result, we have concluded that, carbon coating is one of the important strategies to enhance lithium ion diffusion by increasing the electronic conductivity of the material.

4. Conclusion

In summary, Co_2SnO_4 particles were successfully synthesized by a sonochemical method and carbon coated Co_2SnO_4 particles were achieved using glucose as a carbon source. The compound formation temperature and pH dependence of compound formation were identified through TGA/DTA and XRD analysis, respectively. TGA analysis showed that 27 wt% of the carbon is coated on the pristine Co_2SnO_4 sample. HRTEM analysis confirms the encapsulation of carbon around the Co_2SnO_4 particles and the coating thickness was measured to be 15 nm. The electrochemical performance suggests the carbon encapsulated Co_2SnO_4 particle shows an excellent cycling stability with the capacity retention of 81% after 20 cycles. From EIS analysis, the reduced charge-transfer resistance obtained for carbon encapsulated Co_2SnO_4 suggested that the enhanced electrochemical performance can be attributed to the improved electrical conductivity.

Acknowledgements

One of the authors (RKS) is grateful to UGC (no. 41-838/2012 (SR)) for their financial support under UGC-MRP.

Notes and references

1 L. Ji, Z. Lin, M. Alcoutlabi and X. Zhang, *Energy Environ. Sci.*, 2011, **4**, 2682.
2 M. Holpapfel, H. Buqa, W. Scheifele, P. Novak and F. M. Petrat, *Chem. Commun.*, 2005, 1566.
3 C. M. Park, J. H. Kim, H. Kim and H. J. Sohn, *Chem. Soc. Rev.*, 2010, **39**, 3115.
4 J. Cabana, L. Monconduit, D. Larcher and M. R. Palacin, *Adv. Mater.*, 2010, **22**, E170.
5 N. Du, Y. Xu, H. Zhang, J. Yu, C. Zhai and D. Yang, *Inorg. Chem.*, 2011, **50**, 3320.
6 J. Li, S. Xiong, Y. Liu, Z. Ju and Y. Qian, *ACS Appl. Mater. Interfaces*, 2013, **5**, 981–988.
7 P. Lavala, J. L. Tirado and T. Vidal-Abarca, *Electrochim. Acta*, 2007, **52**, 7986.
8 L. Zhou, H. B. Wu, T. Zhu and X. W. Lou, *J. Mater. Chem.*, 2012, **22**, 827.
9 L. Hu, H. Zhong, X. Zheng, Y. Haung, P. Zhang and Q. Chen, *Sci. rep.*, 2012, **2**, 986.
10 Y. Ding, Y. Yang and H. Shao, *Electrochim. Acta*, 2011, **56**, 9433.
11 P. Lavela and J. L. Tirado, *J. Power Sources*, 2007, **172**, 379.
12 F. Belliard and J. T. S. Irvine, *J. Power Sources*, 2001, **97-98**, 219.
13 S. M. Becker, M. Scheuermann, V. Seplek, A. Eichhofer, D. Chen, R. Monig, A. S. Ulrich and S. Indris, *Phys. Chem. Chem. Phys.*, 2011, **13**, 19624.
14 A. Rong, X. P. Gao, G. R. Li, T. Y. Yan, H. Y. Zhu, J. Q. Qu and D. Y. Song, *J. Phys. Chem. B*, 2006, **110**, 14754.
15 S. J. Lei, K. B. Tang, C. H. Chen, Y. Jin and L. Zhou, *Mater. Res. Bull.*, 2009, **44**, 393.
16 G. Wang, X. P. Gao and P. W. Shen, *J. Power Sources*, 2009, **192**, 719.
17 F. Haung, Z. Y. Yuan, H. Zhan, Y. H. Zhou and J. T. Sun, *Mater. Lett.*, 2003, **57**, 3341.
18 Z. Wang, Z. Wang, W. Liu, W. Xiao and X. W. Lou, *Energy Environ. Sci.*, 2013, **6**, 87.
19 Y. Qi, H. Zhang, N. Du, C. Zhai and D. Yang, *RSC Adv.*, 2012, **2**, 9511.
20 Y. Zhu, J. Zhang, J. Liang, L. Fan, D. Wei and Y. Qian, *J. Mater. Chem. A*, 2013, DOI: 10.1039/c3ta13228e.
21 J. J. Zhang and Y. Y. Xia, *J. Electrochem. Soc.*, 2006, **153**, A1466.
22 Y. Qi, N. Du, H. Zhang, P. Wu and D. Yang, *J. Power Sources*, 2011, **196**, 10234.
23 R. Alcantara, G. F. Ortiz, P. Lavela and J. L. Tirado, *Electrochem. Commun.*, 2006, **8**, 731.
24 A. Shamirian, M. Edrisi and M. Nadevi, *J. Mater. Eng. Perform.*, 2013, **22**, 306–311.
25 J. A. Aguilar-Martinez, M. I. Pech-Canuel, M. Esneider, A. Toxgui and S. Shaji, *Mater. Lett.*, 2012, **78**, 28–31.
26 L. Su, Y. Jing and Z. Zhou, *Nanoscale*, 2011, **3**, 3967.
27 C. F. Baes and R. E. Mesmer, *The hydrolysis of cations*, Wiley Interscience, Newyork, 1976.
28 J. Burges, *Metal Ions of Cations*, Ellis Horwood, Chichester, England, 1978, p. 264.
29 J. Livage, *Materials*, 2010, **3**, 4175–4195.
30 M. Henry, J. P. Jolivet and J. Livage, *Struct. Bonding*, 1992, **77**, 154.
31 Z. P. Xu and H. C. Zeng, *J. Mater. Chem.*, 1998, **8**(11), 2499.
32 M. Al-Ghoul, H. EI-Rassy, T. Coradin and T. Mokalled, *J. Crys. Growth*, 2010, **312**, 856.
33 E. W. Giesekke, H. S. Gutowsky, P. Kirkov and H. A. Laitinen, *Inorg. Chem.*, 1967, **6**, 1294.
34 H. Yang, J. Ouyang and A. Tang, *J. Phys. Chem. B*, 2007, **111**, 8006.
35 L. M. Fang, X. T. Zu, Z. J. Li, S. Zhuc, C. M. Liu, W. L. Zhou and L. M. Wang, *J. Alloys Compd.*, 2008, **454**, 261.
36 W. Wang, C. Xu, X. Wang, Y. Liu, Y. Zhan, C. Zheng, F. Song and G. Wang, *J. Mater. Chem.*, 2002, **12**, 1922.
37 D. L. Pavia, G. M. Lampman and G. S. Kriz, *Introduction to spectroscopy*, Harcourt publishers, 2009, p. 16.
38 S. Ikeda, K. Tachi, Y. H. Ng, Y. Ikoma, T. Sakata, H. Mori, T. Harada and M. Matsumura, *Chem. Mater.*, 2007, **19**, 4335.
39 L. Xu, W. Zhang, Y. Ding, Y. Peng, S. Zhang, W. Yu and Y. Qian, *J. Phys. Chem. B*, 2004, **108**, 10859.
40 R. Baddour-Hadjean and J.-P. Pereira-Ramos, *Chem. Rev.*, 2010, **110**, 1278.
41 D. Bresser, E. Paillard, R. Kloepsch, S. Krueger, M. Fielder, R. Schmitz, D. Baither, M. Winter and S. Passerini, *Adv. Energy Mater.*, 2013, **3**, 513.
42 C. He, S. Wu, N. Zhao, C. Shi, E. Liu and J. Li, *ACS Nano*, 2013, **7**, 4459.
43 Y. Sharma, N. Sharma, G. V. Subba Rao and B. V. R. Chowdari, *Solid State Ionics*, 2008, **179**, 587.
44 L. Li, S. Peng, J. Wang, Y. Ling Cheah, P. The, Y. Ko, C. Wong and M. Srinivasan, *ACS Appl. Mater. Interfaces*, 2012, **4**(11), 6005.
45 J. F. Marco, J. R. Gancedo, M. Gracia, J. L. Gautier, E. I. Rios and F. J. Berry, *J. Solid State Chem.*, 2000, **153**, 74.
46 J. Yan, B. Xia, Y. Su, X. Zhou, J. Zhang and X. Zhang, *Electrochim. Acta*, 2008, **53**, 7069.
47 J. Yan, J. Zhang, Y. Su, X. Zhang and B. Xia, *Electrochim. Acta*, 2010, **55**, 1785.
48 S. Chattopadhyay, A. L. Lipson, H. J. Karmel, J. D. Emery, T. T. Fister, P. A. Fenter, M. C. Hersan and M. J. Bedzyk, *Chem. Mater.*, 2012, **24**, 3038.
49 Y. Qi, N. Du, H. Zhang and D. Yang, *J. Power Sources*, 2011, **196**, 10234.
50 G. Wang, Z. Y. Liu and P. Liu, *Electrochim. Acta*, 2011, **56**, 9515.
51 D. W. Jung, S. W. Han, J. H. Jeong and E. S. Oh, *J. Electroanal. Chem.*, 2013, **695**, 30.
52 R. Alcandara, G. F. Ortiz, R. Lavela and J. L. Tirado, *Electrochem. Commun.*, 2006, **8**, 731.
53 N. Munichandraiah, L. G. Scanlon and R. R. Marsh, *J. Power Sources*, 1998, **72**, 203.
54 L. Lang and Z. Xu, *ACS Appl. Mater. Interfaces*, 2013, **5**, 1698.
55 H. Li, Z. Wang, L. Chen and X. Huang, *Adv. Mater.*, 2009, **21**, 4593.
56 L. Su, Y. Jing and Z. Zhou, *Nanoscale*, 2011, **3**, 3967.
57 Y. Sharma, N. Sharma, G. V. Subba Rao and B. V. R. Chowdari, *Chem. Mater.*, 2008, **20**, 6829.

58 J. Zhu, Y. K. Sharma, Z. Zeng, X. Zhang, M. Srinivasan, S. Mhaisalkar, H. Zhang, H. H. Hng and Q. Yan, *J. Phys. Chem. C*, 2011, **115**, 8400–8406.
59 M. C. Smart, B. V. Ratnakumar, S. Surampudi, Y. Wang, X. Zhang, S. G. Greenbaum, A. Hightower, C. C. Ahn and B. Fultz, *J. Electrochem. Soc.*, 1999, **146**(11), 3963.
60 C. He, S. Wu, N. Zhao, C. Shi, E. Liu and J. Li, *ACS Nano*, 2013, **7**, 4459.
61 X. L. Wu, Y. G. Guo, J. Su, J. W. Xiong, Y. L. Zhang and L. J. Wan, *Adv. Energy Mater.*, 2013, **3**, 1155.
62 X. Chen, N. Q. Zhang and K. N. Sun, *J. Phys. Chem.C.*, 2012, **116**, 21224.